Packet narrowing and quantum entanglement in photoionization and photodissociation

M. V. Fedorov,[1,*] M. A. Efremov,[1] A. E. Kazakov,[1] K. W. Chan,[2,†] C. K. Law,[3] and J. H. Eberly[2]
[1]*General Physics Institute, Russian Academy of Sciences, 38 Vavilov Street, Moscow 119991, Russia*
[2]*Center for Quantum Information and Department of Physics and Astronomy, University of Rochester, Rochester, New York 14627, USA*
[3]*Department of Physics, The Chinese University of Hong Kong, NT, Hong Kong SAR, China*
(Received 5 December 2003; published 26 May 2004)

The narrowing of electron and ion wave packets in the process of photoionization is investigated, with the electron-ion recoil taken fully into account. Packet localization of this type is directly related to entanglement in the joint quantum state of the electron and ion, and to Einstein-Podolsky-Rosen localization. Experimental observation of such packet-narrowing effects is suggested via coincidence registration by two detectors, with a fixed position of one and varying position of the other. A similar effect, typically with an enhanced degree of entanglement, is shown to occur in the case of photodissociation of molecules.

DOI: 10.1103/PhysRevA.69.052117 PACS number(s): 03.65.Ud, 03.67.Hk, 39.20.+q

I. INTRODUCTION

Photoionization of atoms has been treated repeatedly in both weak and strong fields (see, for example, [1] and [2]). Most often in the theoretical analysis of these processes it is assumed that the atomic center of mass has a given and well defined position $\vec{r}_0$ and that the atomic mass is infinitely large. Obviously, neither of these two assumptions is rigorously true. In this work we consider photoionization of an atom with a single valence electron and with the relative electron-ion motion and the atomic center-of-mass motion described by wave functions with finite widths, both before and after ionization. Such a formulation of the problem gives rise to some interesting questions related to the entanglement of electron-ion quantum states.

Entanglement of quantum states is of fundamental interest and is also closely related to questions arising in photoionization because the fragmentation process that occurs in photoionization is a concrete realization of the one used by Einstein, Podolsky, and Rosen (EPR) [3] to illustrate Einstein's ideas regarding the limitations of quantum theory. By definition, entanglement means nonfactorization of a two-particle wave function. Mathematically, for such a function the degree of entanglement can be compactly characterized by the Schmidt number [4], denoted $K=[\mathrm{Tr}(\rho^2)]^{-1}$, where ρ is the reduced density matrix of either one of the two particles under consideration. For background on Schmidt-based analysis, a number of overviews exist [5,6]. In this work we will take a different approach and show that electron-ion entanglement in the process of photoionization is closely related to the evolving spatial wave-packet structures of the electron and ion wave packets.

For experimental investigation of electron-ion entanglement, and for clarification of entanglement physics in the photionization process, we demonstrate the value of making and comparing results from both coincidence (conditioned) and single-particle (unconditioned) observations. In the coincidence scheme the electron and ion positions are assumed to be registered simultaneously by two different detectors, and only joint signals from both detectors are recorded. For example, given the fixed ion detector position $\vec{r}_i$, one scans the electron detector position $\vec{r}_e$ and thus obtains the structure of the electron wave packet as a function of $\vec{r}_e$ as seen in coincidence. In the single-particle scheme only the electron detector is used, and the nature of the electron wave packet is determined as a function of $\vec{r}_e$, irrespective of $\vec{r}_i$. The difference between the results of such scans (i.e., of measurements of packet widths) is a straightforward experimental measure of nonseparability, i.e., of entanglement.

Specifically, to characterize this difference in a quantitative fashion, we will use the ratio R of the wave-packet widths found in the single-particle and coincidence schemes. There will be two such ratios R_e and R_i for electron and ion and they will be shown to be equal in situations of interest, allowing us to put $R_e=R_i\equiv R$, and the parameter R will be referred to as the entanglement parameter. Compared to the Schmidt correlation coefficient K the parameter R describes more detailed time-evolving features of entangled quantum states. In particular, in the coordinate picture that we use here, changes in the parameter R occur because of spreading of electron and ion wave packets after ionization. The time evolution of $R(t)$ efficiently separates two significantly different entanglement regimes. For factorized two-particle states, when there is no entanglement, both K and R take their minimal values equal to 1. For $R>1$ the quantum state under consideration must be entangled, i.e., nonfactorized. But this statement cannot be inverted: there is a special kind of entangled quantum state, in which $R=1$. All these situations are described below for photoionization, and we briefly discuss similar issues for dissociation of a diatomic molecule and explain the most significant differences in the results.

In contrast to other treatments of fragmentation or "breakup" [7], the coordinate-picture wave-packet analysis gives an alternative view of entanglement and reveals additional channels for achieving high degrees of entanglement. In addition to the entanglement parameter R we also identify

*Electronic address: fedorov@ran.gpi.ru
†Electronic address: kwchan1@pas.rochester.edu

"control parameters" for comparison with those that have been advanced in previous studies of both photon-atom [8,9] and photon-photon [10,11] wave functions, and through conditional localization our approach is related to formal photonic analogs [12] of the EPR discussion and also diatomic breakup as a route to matter wave entanglement [13].

II. PHOTOIONIZATION

Let an atom, originally in its ground state, be photoionized by a light field

$$\vec{\mathcal{E}}(t) = \vec{\mathcal{E}}_0 \sin(\omega t), \tag{1}$$

where $\hbar\omega > |E_0|$ and E_0 is the ground state energy. It should be noted that by using the dipole approximation and ignoring the term $\vec{k}\cdot\vec{r}$ in the argument in Eq. (1) we are ignoring all recoil effects due to absorption of the photon momentum $\hbar\vec{k}$. This approximation is quite reasonable, because there is another much stronger mechanism giving rise to recoil. In the process of photoionization an atomic electron acquires an energy $\sim\hbar\omega$ and hence a momentum $\sim\sqrt{m\hbar\omega}$, and the ion gets the same momentum (with the opposite sign), and this momentum is much larger than $\hbar k = \hbar\omega/c$. This is in contrast to the problems of entanglement in spontaneous photon emission of excited atoms and Raman scattering [8].

To describe such a process with atomic recoil and with an initial wave-packet distribution of the atomic center of mass, let us begin from the Schrödinger equation for two particles—electron and ion—in the field. Traditionally, to separate variables in such an equation, we use the relative (rel) and center-of-mass (c.m.) position and momentum vectors [14]

$$\vec{r}_{\rm rel} = \vec{r}_e - \vec{r}_i, \quad \vec{r}_{\rm c.m.} = \frac{m_e\vec{r}_e + m_i\vec{r}_i}{M},$$
$$\vec{p}_{\rm rel} = \frac{m_i\vec{p}_e - m_e\vec{p}_i}{M}, \quad \vec{p}_{\rm c.m.} = \vec{p}_e + \vec{p}_i, \tag{2}$$

where $\vec{r}_e$ and $\vec{r}_i$ are the electron and ion position vectors, $\vec{p}_e = -i\hbar\partial/\partial\vec{r}_e$ and $\vec{p}_i = -i\hbar\partial/\partial\vec{r}_i$ are their momenta, and m_e and m_i are their masses, with $M = m_e + m_i$. It is worth noting that the "mixed" coordinate-momentum variable pairs $\vec{r}_{\rm rel}$ and $\vec{p}_{\rm c.m.}$, as well as $\vec{r}_{\rm c.m.}$ and $\vec{p}_{\rm rel}$, each have zero commutator. For example, $[\vec{r}_{\rm rel}, \vec{p}_{\rm c.m.}] = 0$. For this reason one can call them EPR pairs, recalling the famous discussion of Einstein, Podolsky, and Rosen [3].

The Schrödinger equation takes the form

$$i\hbar\frac{\partial\Psi}{\partial t} = \left\{\frac{\vec{p}^{\,2}_{\rm c.m.}}{2M} + \frac{\vec{p}^{\,2}_{\rm rel}}{2\mu} - \frac{e^2}{r_{\rm rel}} + e\vec{r}_{\rm rel}\cdot\vec{E}_0\sin(\omega t)\right\}\Psi, \tag{3}$$

where $\mu = m_e m_i/M$ is the reduced mass. Because we have made the dipole approximation, the variables $\vec{r}_{\rm rel}$ and $\vec{r}_{\rm c.m.}$ in Eq. (3) are separated, and its solution is a product of functions depending on these two variables separately:

$$\Psi(\vec{r}_{\rm rel}, \vec{r}_{\rm c.m.}, t) = \Psi_{\rm c.m.}(\vec{r}_{\rm c.m.}, t) \times \Psi_{\rm rel}(\vec{r}_{\rm rel}, t), \tag{4}$$

where the equations of motion of $\Psi_{\rm c.m.}(\vec{r}_{\rm c.m.}, t)$ and $\Psi_{\rm rel}(\vec{r}_{\rm rel}, t)$ are

$$i\hbar\frac{\partial\Psi_{\rm c.m.}}{\partial t} = \frac{\vec{p}^{\,2}_{\rm c.m.}}{2M}\Psi_{\rm c.m.} \tag{5}$$

and

$$i\hbar\frac{\partial\Psi_{\rm rel}}{\partial t} = \left\{\frac{\vec{p}^{\,2}_{\rm rel}}{2\mu} - \frac{e^2}{r_{\rm rel}} + e\vec{r}_{\rm rel}\cdot\vec{\mathcal{E}}_0\sin(\omega t)\right\}\Psi_{\rm rel}. \tag{6}$$

We note that the factorization shown in Eq. (4) is far from the same as factorization in the particle variables $\vec{r}_e$ and $\vec{r}_i$. That is, the electron and ion are quantum entangled in the state given in Eq. (4).

Let us assume that the initial atomic center-of-mass wave function is given by a Gaussian wave packet with width $\Delta r^{(0)}_{\rm c.m.}$:

$$\Psi_{\rm c.m.}(\vec{r}_{\rm c.m.}, t=0) = \frac{1}{(2\pi)^{3/4}[\Delta r^{(0)}_{\rm c.m.}]^{3/2}}\exp\left(-\frac{\vec{r}^{\,2}_{\rm c.m.}}{4[\Delta r^{(0)}_{\rm c.m.}]^2}\right). \tag{7}$$

Then, as is well known [2], the time-dependent solution of Eq. (5) has the form of a spreading wave packet such that

$$|\Psi_{\rm c.m.}(\vec{r}_{\rm c.m.}, t)|^2 = \frac{1}{(2\pi)^{3/2}[\Delta r_{\rm c.m.}(t)]^3}\exp\left(-\frac{\vec{r}^{\,2}_{\rm c.m.}}{2[\Delta r_{\rm c.m.}(t)]^2}\right), \tag{8}$$

where $\Delta r_{\rm c.m.}(t)$ is the time-dependent width of the center-of-mass wave packet (8),

$$\Delta r_{\rm c.m.}(t) = \left\{[\Delta r^{(0)}_{\rm c.m.}]^2 + \frac{\hbar^2 t^2}{4M^2[\Delta r^{(0)}_{\rm c.m.}]^2}\right\}^{1/2} \approx \begin{cases}\Delta r^{(0)}_{\rm c.m.}, & t \ll t^{\rm (c.m.)}_{\rm spr} \\ \dfrac{\hbar t}{2M\ \Delta r^{(0)}_{\rm c.m.}}, & t \gg t^{\rm (c.m.)}_{\rm spr}\end{cases} \tag{9}$$

and $t^{\rm (c.m.)}_{\rm spr}$ is its spreading time, $t^{\rm (c.m.)}_{\rm spr} = 2M[\Delta r^{(0)}_{\rm c.m.}]^2/\hbar$. At $t \gg t^{\rm (c.m.)}_{\rm spr}$ the width $\Delta r_{\rm c.m.}(t)$ grows linearly and the velocity of spreading is given by $v^{\rm (c.m.)}_{\rm spr} = \hbar/2M\Delta r^{(0)}_{\rm c.m.}$.

Under the conditions of interest here, the solution of Eq. (6) is only a little bit more complicated. The initial wave function of the relative motion is taken to be the hydrogen ground state 1*s* wave function

$$\Psi_{\rm rel}(\vec{r}_{\rm rel}, t=0) = \psi_{1s} \equiv R_{10}(r_{\rm rel})Y_{00}, \tag{10}$$

where $R_{10}(r_{\rm rel})$ is the hydrogen radial wave function for the principal quantum number $n=1$ and angular momentum $l=0$, and $Y_{00} = 1/\sqrt{4\pi}$ is the spherical function for $l = m_l = 0$.

We assume a sufficiently high photon energy $\hbar\omega$ to ignore bound-bound transitions. Then the time-dependent wave function obeying Eq. (6) can be presented in the form

$$\Psi_{\rm rel}(\vec{r}_{\rm rel},t) = C_0(t)\psi_{1s} + e^{-i\omega t}\int_0^\infty dE\ C_E(t)\psi_{Ep}, \qquad (11)$$

where ψ_{Ep} is the field-free wave function of the continuous spectrum with $l=1$, $m_l=0$:

$$\psi_{Ep}(\vec{r}_{\rm rel}) = R_{E1}(r_{\rm rel})Y_{10}(\cos\ \theta_{\rm rel}), \qquad (12)$$

in which $R_{E1}(r_{\rm rel})$ is the radial wave function for energy E and angular momentum $l=1$, $Y_{10}=\sqrt{3/4\pi}\cos\ \theta_{\rm rel}$, and $\theta_{\rm rel}$ is the angle between the vectors $\vec{\mathcal{E}}_0$ and $\vec{r}_{\rm rel}$.

With multiphoton processes ignored, the equations of motion for the probability amplitudes $C_0(t)$ and $C_E(t)$ in the rotating-wave approximation, following directly from Eq. (6), are given by

$$i\hbar\dot{C}_0(t) - E_0\ C_0(t) = -\int_0^\infty dE\frac{\vec{d}_{0E}\cdot\vec{\mathcal{E}}_0}{2}C_E(t), \qquad (13a)$$

$$i\hbar\dot{C}_E(t) - (E-\hbar\omega)C_E(t) = -\frac{\vec{d}_{E0}\cdot\vec{\mathcal{E}}_0}{2}C_0(t), \qquad (13b)$$

where $\vec{d}_{E0}=(\vec{d}_{0E})^*$ are the bound-free dipole matrix elements of the atom, and we consider the case of a pulse with rectangular envelope, which means that the interaction is turned on suddenly at $t=0$.

With the help of adiabatic elimination of the continuum [2], Eq. (13a) can be reduced to a much simpler form:

$$i\hbar\dot{C}_0(t) - (E_0 - i\hbar\gamma_I)C_0(t) = 0, \qquad (14)$$

in which the amplitude decay rate γ_I is half the Fermi golden rule rate of ionization:

$$2\gamma_I \equiv \frac{dw_I}{dt} = \frac{2\pi}{\hbar}\left|\langle E|\frac{\vec{d}\cdot\vec{\mathcal{E}}_0}{2}|0\rangle\right|^2_{E=E_{0+\omega}}. \qquad (15)$$

The solution satisfying the initial condition $C_0(0)=1$ is

$$C_0(t) = \exp\left(-\frac{i}{\hbar}E_0 t - \gamma_I t\right). \qquad (16)$$

With this function substituted into the right-hand side of Eq. (13b), the equation for $C_E(t)$ can be easily solved to give, with the initial condition $C_E(0)=0$

$$C_E(t) = \frac{1}{2}\frac{\vec{d}_{E0}\cdot\vec{\mathcal{E}}_0}{E-E_0-\hbar\omega+i\gamma_I} \times\left\{\exp\left[-\left(\frac{iE_0}{\hbar}+\gamma_I\right)t\right] - \exp\left[-i\left(\frac{E}{\hbar}-\omega\right)t\right]\right\}. \qquad (17)$$

At times $t\gg\gamma_I^{-1}$ both $C_0(t)$ in Eq. (16) and the first exponential term in Eq. (17) vanish. As a result the wave function $\Psi_{\rm rel}$ describing relative motion takes the form

$$\Psi_{\rm rel}(\vec{r}_{\rm rel},t) = \frac{-\sqrt{3}}{4\sqrt{\pi}}\cos\ \theta_{\rm rel}\int_0^\infty dE\ R_{E1}(r_{\rm rel}) \times\exp\left(-\frac{i}{\hbar}Et\right)\frac{\vec{d}_{E0}\cdot\vec{\mathcal{E}}_0}{E-E_0-\hbar\omega+i\hbar\gamma_I}. \qquad (18)$$

We assume that the laser frequency ω and hence the energy $E\sim E_0+\hbar\omega$ are high enough so that the radial function $R_{E1}(r_{\rm rel})$ is approximated by the well known high-energy field-free expression for the Coulomb radial wave function [14]:

$$R_{E1}(r) \approx \sqrt{\frac{2\mu}{\pi k}}\frac{1}{\hbar r}\cos\left(kr + \frac{1}{ka_0}\ln(2kr) + \delta_1\right), \qquad (19)$$

where $k=\sqrt{2\mu E}/\hbar$, δ_1 is the Coulomb scattering phase for $l=1$, and $a_0=\hbar^2/\mu e^2$ is the Bohr radius.

When the photoelectrons have energy far above the continuum threshold, we have $\hbar\gamma_I \ll E\sim E_0+\omega$. In this way the lower limit of the integration over E in Eq. (18) can be replaced by $-\infty$. The energy E is approximated by $E_*\equiv E_0+\hbar\omega$ in all the preexponential factors except the denominator on the right-hand side of Eq. (18). Also, both the scattering phase δ_1 and logarithmic term in the argument of cosine in Eq. (19) are neglected, and the factor k in the product kr is expanded in powers of $E-E_*$, *viz.* $k\approx k_*+(E-E_*)/\hbar v$, where $k_*=\sqrt{2\mu E_*}/\hbar$ and $v=\sqrt{2E_*/\mu}=\hbar k_*/\mu$ is the velocity of the relative motion. Then the integral over E can be evaluated by the residue method, giving

$$\Psi_{\rm rel} = \frac{i\sqrt{6}}{4\sqrt{\hbar v}}\left(\vec{d}_{E_*0}\cdot\vec{\mathcal{E}}_0\right)\exp\left(-i\frac{E_* t}{\hbar}+ik_* r_{\rm rel}\right) \times\frac{\cos\ \theta_{\rm rel}}{r_{\rm rel}}\exp\left[-\gamma_I\left(t-\frac{r_{\rm rel}}{v}\right)\right]\theta(vt-r_{\rm rel}). \qquad (20)$$

This equation describes a spherical wave packet in $r_{\rm rel}$ with an angular modulation determined by the factor $\cos\ \theta_{\rm rel}$, propagating in the direction of growing $r_{\rm rel}$ with velocity v, and having a sharp edge at $r_{\rm rel}=vt$ and an exponentially falling tail at $r_{\rm rel}<vt$. The radial width of the wave packet (20) is $v/2\gamma_I$.

III. FURTHER EVOLUTION OF THE RELATIVE-MOTION WAVE FUNCTION

Although we have assumed that the time t exceeds the total ionization time ($t>\gamma_I^{-1}$), Eq. (20) still describes the initial stage for the relative-motion wave-packet evolution after ionization. In this sense $v/2\gamma_I$ is the initial width of the relative-motion wave packet $|\Psi_{\rm rel}|^2$, which we denote by $\Delta r_{\rm rel}^{(0)}\equiv v/2\gamma_I$. This width can change later due to dispersion. To describe such a spreading effect, we can extend our series expansion of the function $k(E)$ up to second order in $E-E_*$: $k\approx k_*+(E-E_*)/\hbar v-(E-E_*)^2/2\hbar\mu v^3$. This gives rise to an additional factor in the integral over the energy E: $\exp\{-i\,E^2 r_{\rm rel}/2\hbar\mu v^3\}$. To keep the possibility of integration by the residue method, we have to use the Fourier transformation of this factor:

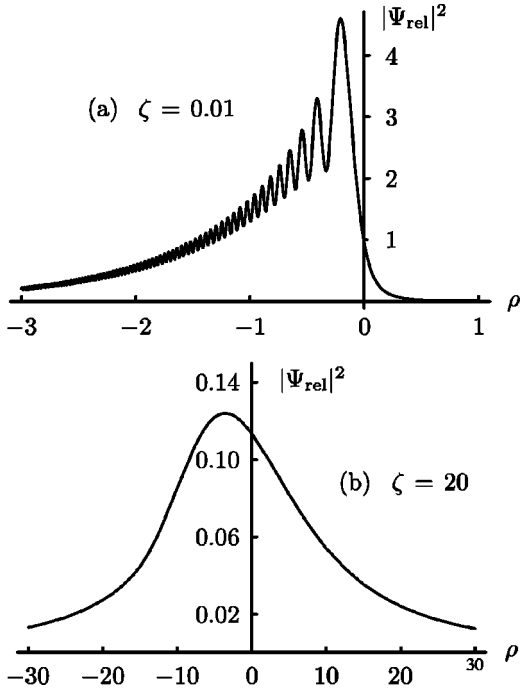

FIG. 1. The relative-motion probability density $|\Psi_{\rm rel}|^2$ (21) in dependence on $\rho=(r_{\rm rel}-vt)/\Delta r_{\rm rel}^{(0)}$ at (a) $\zeta=0.01$ and (b) $\zeta=20$.

$$\exp\left\{-i\frac{E^2 r_{\rm rel}}{2\hbar\mu v^3}\right\}=\sqrt{\frac{\mu v^3}{2\pi i\hbar r_{\rm rel}}}\int_{-\infty}^{\infty}d\tau \times\exp\left\{\frac{i}{\hbar}\left[E\tau+\frac{\mu v^3\tau^2}{2r_{\rm rel}}\right]\right\}.$$

With this representation we first carry out the integration over E (by the residue method) and then the one over τ. The result is

$$|\Psi_{\rm rel}(r_{\rm rel},t)|^2=\frac{3}{16\pi\,\Delta r_{\rm rel}^{(0)}}\frac{\cos^2\theta_{\rm rel}}{r_{\rm rel}^2}\exp\left(\frac{r_{\rm rel}-vt}{\Delta r_{\rm rel}^{(0)}}\right)\times\left|1-{\rm Erf}\left[\sqrt{\frac{i}{2}}\left(\frac{\sqrt{\zeta}}{2}-\frac{i}{\sqrt{\zeta}}\frac{r_{\rm rel}-vt}{\Delta r_{\rm rel}^{(0)}}\right)\right]\right|^2, \tag{21}$$

where Erf is the error function, and we have defined

$$\zeta\equiv\frac{\hbar r_{\rm rel}}{v\mu(\Delta r_{\rm rel}^{(0)})^2}\equiv\frac{r_{\rm rel}}{vt_{\rm spr}}, \tag{22}$$

so that $t_{\rm spr}^{\rm (rel)}=\mu(\Delta r_{\rm rel}^{(0)})^2/\hbar$ is the spreading time of the relative-motion wave packet. As the value of $|\Psi_{\rm rel}|^2$ is concentrated around $r_{\rm rel}\approx vt$, by putting $r_{\rm rel}\approx vt$ in the definition of the parameter ζ, we get $\zeta=t/t_{\rm spr}^{\rm (rel)}$. In this form the meaning of ζ is obvious: it is the time after ionization measured in units of the spreading time of the relative-motion wave packet. In Figs. 1(a) and 1(b) the function $|\Psi_{\rm rel}|^2$ is plotted in its dependence on $\rho\equiv(r_{\rm rel}-vt)/\Delta r_{\rm rel}^{(0)}$ at small and large ζ's, respectively.

In the small-spreading regime $(\zeta\ll1)$ $|\Psi_{\rm rel}|^2$ returns to the form of Eq. (20), but with additional oscillations on the left wing and a slightly smoothed right wing as compared to the step function jump of Eq. (20). In the large-spreading regime $(\zeta\gg1)$ $|\Psi_{\rm rel}|^2$ approaches a Lorentzian shape:

$$|\Psi_{\rm rel}|^2=\frac{3}{8\pi^2}\frac{\cos^2\theta_{\rm rel}}{r_{\rm rel}^2}\frac{\Delta r_{\rm rel}(t)}{(r_{\rm rel}-vt)^2+\frac{1}{4}[\Delta r_{\rm rel}(t)]^2}, \tag{23}$$

where

$$\Delta r_{\rm rel}(t)=\zeta\,\Delta r_{\rm rel}^{(0)}=\frac{t}{t_{\rm spr}}\,\Delta r_{\rm rel}^{(0)}=v_{\rm spr}t \tag{24}$$

and $v_{\rm spr}\equiv\Delta r_{\rm rel}^{(0)}/t_{\rm spr}=\hbar/\mu\Delta r_{\rm rel}^{(0)}$. Altogether, at small and large ζ, the time-dependent width of the relative-motion wave packet is given by

$$\Delta r_{\rm rel}(t)=\begin{cases}\Delta r_{\rm rel}^{(0)}=\dfrac{v}{2\gamma_I}, & t\ll t_{\rm spr}^{\rm (rel)}(\zeta\ll1),\\ v_{\rm spr}t=\dfrac{\hbar t}{\mu\,\Delta r_{\rm rel}^{(0)}}=\dfrac{2\hbar\gamma_I}{\mu v}t, & t\gg t_{\rm spr}^{\rm (rel)}(\zeta\gg1).\end{cases} \tag{25}$$

In spite of clear differences between the Gaussian center-of-mass (8) and relative-motion (20),(21),(23) wave packets, their widths behave similarly in their dependence on t: they start from initial values $\Delta r_{\rm c.m.}^{(0)}$ and $\Delta r_{\rm rel}^{(0)}$, and at times longer than the corresponding spreading times both $\Delta r_{\rm rel}(t)$ and $\Delta r_{\rm c.m.}(t)$ grow linearly. In both cases the spreading time is proportional to the squared initial size, and the velocity of spreading is inversely proportional to the initial size. The only qualitative difference is the mass: the total mass M appears in the center-of-mass wave function, but the relative-motion wave packet depends on the reduced mass μ.

The relation between the center-of-mass and relative-motion wave-packet widths can change with time due to different spreading velocities of these wave packets. This makes the time evolution of the electron-ion wave function rather complicated, and this problem will be discussed separately in Sec. V.

IV. LOCALIZATION OF THE ELECTRON-ION WAVE PACKET AND ENTANGLEMENT

In accord with Eq. (4), the product of the wave functions given in Eqs. (8) and (21) determines the total wave function of the ion-electron system. It should now be considered as a function of ion and electron position vectors

$$\Psi(\vec{r}_e,\vec{r}_i,t)=\Psi_{\rm c.m.}\left(\frac{m_e\vec{r}_e+m_i\vec{r}_i}{M},t\right)\times\Psi_{\rm rel}(\vec{r}_e-\vec{r}_i,t), \tag{26}$$

showing that both Ψ and its squared absolute value are not factorable in the individual particle coordinates $\vec{r}_e$ and $\vec{r}_i$. Such nonfactorization defines quantum particle entanglement of the electron and ion.

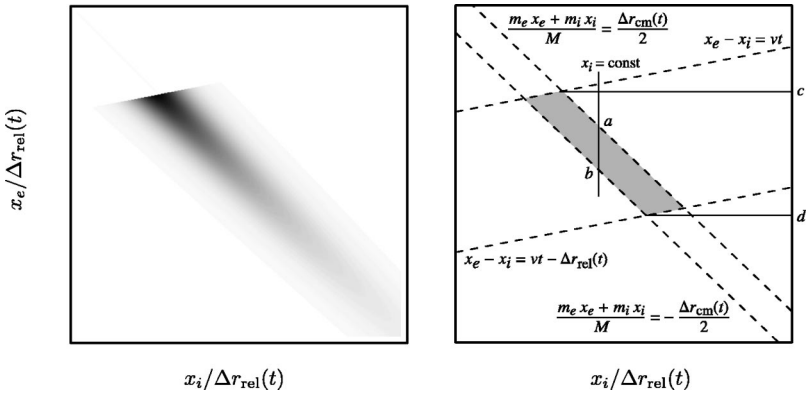

FIG. 2. The density distribution of the one-dimensional equivalent of $|\Psi|^2$ given in Eq. (26), where x_e and x_i are the one-dimensional electron and ion coordinates. The left picture corresponds to $\Psi_{\rm c.m.}$ and $\Psi_{\rm rel}$ of Eq. (26) given by Eqs. (8) and (21), with $\vec{r}_e$ and $\vec{r}_i$ substituted by x_e and x_i. In the right picture $\Psi_{\rm c.m.}$ and $\Psi_{\rm rel}$ are modeled by sharp-edged flat functions, with boundaries of their localization regions shown by the dashed lines. The difference between the single-particle and coincidence-scheme widths of the electron wave packets is illustrated by the difference between the *cd* and *ab* distances in the right picture. This difference and the value of the entanglement parameter are seen to be large for a large aspect ratio of the shaded region. We have used $m_e/m_i=0.2$, $\eta=0.5$, and $\gamma_1 t=4$ for illustration.

We will proceed by examining the relationship of entanglement to the ratio of widths

$$\eta(t) \equiv \frac{\Delta r_{\rm c.m.}(t)}{\Delta r_{\rm rel}(t)} \tag{27}$$

where the time t is taken as a parameter. Note that in our treatment $\eta(t)$ is constrained only by momentum and energy conservation (e.g., we ignore final-state electron-ion Coulomb effects). Here $\Delta r_{\rm c.m.}(t)$ is of kinematic origin whereas $\Delta r_{\rm rel}(t)$ is due to the dynamics of the ionization process. We will see that $\eta(t)$ acts as a useful control parameter for entanglement of the two-particle system.

In cases of two-particle fragmentation or "breakup," as in photoionization, and where significant further interaction is absent, measures of entanglement can be related to a series of spatial localization measurements. Such a connection to potential experiments was not treated in earlier studies of photon-atom or photon-photon breakup processes like spontaneous photon emission with atom recoil [8,9] or parametric down-conversion [10,11], but is related to the measurement-induced localization and entanglement discussed recently in a very different context by Rau *et al.* [15].

Now we focus on measurements appropriate for seeing entanglement. We need to distinguish coincidence and noncoincidence (single-particle) measurements, which have their theoretical counterparts in conditional and nonconditional probability distributions. For an example of a single-particle measurement, the electron probability distribution is measured regardless of the ion position (or vice versa). In contrast, a coincidence measurement assumes that a distribution of electron positions is registered while the ion detection position is kept at a given (constant) location (or vice versa). The difference between the results of coincidence and single-particle schemes of measurements is illustrated by Fig. 2. In this picture, in one dimension, we shade the region in which the joint probability density $|\Psi(\vec{r}_e,\vec{r}_i,t)|^2$ is significant. In the left plot the sharp leading edge of the theta function in Eq. (20) is apparent, with its long exponential tail, and one also sees the more abrupt Gaussian cutoff on the sides. A purely schematic view of the same thing is shown in the right plot, where artificially sharp dashed-line borders are introduced and are supposed to be determined by the localization zones of the relative-motion and center-of-mass wave functions.

Consider first an examination of the electron wave packet by the coincidence-scheme method, for a given ion coordinate $x_i=$const. The normalized measure of its width, $\Delta x_e/\Delta r_{\rm rel}(t)$, will be given by the distance between the points marked *a* and *b*. In contrast, the single-particle width takes into account the contributions from all possible different x_i's. Thus a suitable measure of the single-particle width of the electron wave packet is given by the distance *cd*. It is obvious that the electron packet is relatively highly localized when $cd \gg ab$. Correspondingly, a horizontal line through the shaded region would provide a normalized measure of Δx_i, etc. From this sketch we formulate two conditions simultaneously necessary for the entanglement parameter to be large: a high aspect ratio of the shaded area and a diagonal angle between the dashed lines restricting the wave-packet localization zones and the coordinate axes x_e and x_i. The high-aspect-ratio condition means that one of the two wave packets ("c.m." or "rel") is much wider than the other one.

Reflection shows that this is achieved by a very thin packet in $x_i - x_e$ space, e.g., any slightly smoothed version of the limit case $\delta(x_i-\kappa x_e)$ for a finite κ, and the normalized relative information gain is well expressed by the ratio of single to coincidence widths. One can also see that a sketch corresponding to Fig. 2, but for independent particles, has dashed lines that are horizontal and vertical, in which case all x_i's predict exactly the same Δx_e, and vice versa.

Mathematically, single-particle probability densities are given by Eq. (26) integrated over either $\vec{r}_i$ or $\vec{r}_e$:

$$P_e(\vec{r}_e,t) = \int d\vec{r}_i |\Psi(\vec{r}_e,\vec{r}_i,t)|^2 \tag{28}$$

or

$$P_i(\vec{r}_i,t) = \int d\vec{r}_e |\Psi(\vec{r}_e,\vec{r}_i,t)|^2. \tag{29}$$

Such distributions reveal no entanglement effects because all the information about the position of one of the particles is lost completely when the two-particle probability density is integrated over $\vec{r}_i$ or $\vec{r}_e$. However, P_e and P_i do serve a normalization role, as we explain later.

Let $\Delta r_e^{(s)}$ and $\Delta r_i^{(s)}$ be the widths of the single-particle electron and ion wave packets, where, for example, $|\Delta r_e^{(s)}|^2 = \langle|\vec{r}_e|^2\rangle - |\langle\vec{r}_e\rangle|^2$, with

$$\begin{aligned}\langle\vec{r}_e\rangle &= \int d\vec{r}_e\, \vec{r}_e\, P_e(\vec{r}_e,t) \\ &= \int\int d\vec{r}_e\, d\vec{r}_i\, \vec{r}_e\, |\Psi(\vec{r}_e,\vec{r}_i,t)|^2 \\ &= \langle\vec{r}_{\text{c.m.}}\rangle + \frac{m_i}{M}\langle\vec{r}_{\text{rel}}\rangle \end{aligned} \tag{30}$$

and

$$\begin{aligned}\langle|\vec{r}_e|^2\rangle &= \int d\vec{r}_e\, r_e^2\, P_e(\vec{r}_e,t) = \int\int d\vec{r}_e\, d\vec{r}_i\, r_e^2\, |\Psi(\vec{r}_e,\vec{r}_i,t)|^2 \\ &= \left\langle \left| \vec{r}_{\text{c.m.}} + \frac{m_i}{M}\vec{r}_{\text{rel}} \right|^2 \right\rangle = \langle|\vec{r}_{\text{c.m.}}|^2\rangle + 2\frac{m_i}{M}\langle\vec{r}_{\text{c.m.}}\rangle\langle\vec{r}_{\text{rel}}\rangle \\ &\quad + \frac{m_i^2}{M^2}\langle|\vec{r}_{\text{rel}}|^2\rangle. \end{aligned} \tag{31}$$

Note that we have used the relation $\vec{r}_e = \vec{r}_{\text{c.m.}} + m_i/M\vec{r}_{\text{rel}}$ and changed the integration variables to the center-of-mass and relative coordinates. Then Eqs. (30) and (31) yield the single-particle measures

$$\delta r_e^{(s)} \equiv \frac{\Delta r_e^{(s)}}{\Delta r_{\text{rel}}(t)} = \sqrt{\eta^2(t) + \left(\frac{m_i}{M}\right)^2}, \tag{32}$$

and, similarly,

$$\delta r_i^{(s)} \equiv \frac{\Delta r_i^{(s)}}{\Delta r_{\text{rel}}(t)} = \sqrt{\eta^2(t) + \left(\frac{m_e}{M}\right)^2}. \tag{33}$$

Note that the relative-motion wave packet width $\Delta r_{\text{rel}}(t)$ plays the role of a natural normalization factor for both single-particle and coincidence-scheme (see below) electron and ion wave-packet widths. Divided by $\Delta r_{\text{rel}}(t)$, these widths become dimensionless, and they are denoted $\delta r_{e,i}^{(s)}$ and $\delta r_{e,i}^{(c)}$.

In the coincidence scheme of measurements the overall width of the distribution (26) with respect to $\vec{r}_e$ at a fixed $\vec{r}_i$ is given by the smaller of $(M/m_e)\Delta r_{\text{c.m.}}(t)$ and $\Delta r_{\text{rel}}(t)$, which is well represented by a simple formula for the coincidence measures:

$$\delta r_e^{(c)} \equiv \frac{\Delta r_e^{(c)}}{\Delta r_{\text{rel}}(t)} \approx \frac{\eta(t)}{\sqrt{\eta^2(t) + (m_e/M)^2}}. \tag{34}$$

The expression in Eq. (34) is appropriate when we are in one of the extreme cases $(M/m_e)\Delta r_{\text{c.m.}}(t) \gg \Delta r_{\text{rel}}(t)$ or $\ll \Delta r_{\text{rel}}(t)$.

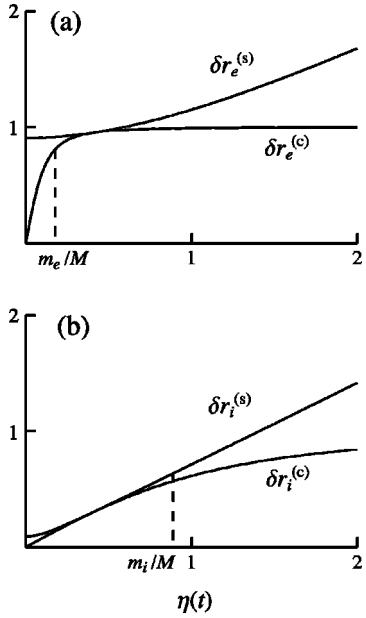

FIG. 3. Electron (a) and ion (b) wave-packet widths in the schemes of single-particle and coincidence measurements with $m_e/m_i = 0.1$.

As shown later in this section, these limits correspond to the high-entanglement regimes of main interest, and we do not need to bother too much about the details of the intermediate region. Similarly, at a given $\vec{r}_e$, the widths of $|\Psi_{\text{c.m.}}|^2$ and $|\Psi_{\text{rel}}|^2$ with respect to $\vec{r}_i$ are correspondingly $(M/m_i)\Delta r_{\text{c.m.}}(t)$ and $\Delta r_{\text{rel}}(t)$. Therefore the overall width of $|\Psi|^2$ at a given $\vec{r}_e$ is the smaller of $(M/m_i)\Delta r_{\text{c.m.}}(t)$ and $\Delta r_{\text{rel}}(t)$, corresponding to the formula

$$\delta r_i^{(c)} \equiv \frac{\Delta r_i^{(c)}}{\Delta r_{\text{rel}}(t)} \approx \frac{\eta(t)}{\sqrt{\eta^2(t) + (m_i/M)^2}}. \tag{35}$$

It is clear now how $\eta(t)$ of Eq. (27) serves as a "control parameter" for both coincidence widths. Plots of $\delta r_e^{(s)}$ and $\delta r_e^{(c)}$ as a function of η are shown in Fig. 3(a) whereas graphs of $\delta r_i^{(s)}$ and $\delta r_i^{(c)}$ are shown in Fig. 3(b). Note that we use in these graphs an artificial value of the electron to ion mass ratio $m_e/m_i = 0.1$ so as to show more clearly the difference between the two curves for $\eta < 1$. However, all the qualitative conclusions from these pictures remain the same for a more realistic value of this ratio $m_e/m_i \sim 10^{-4}$. One of these conclusions is that we always have $\delta r_{e,i}^{(s)} > \delta r_{e,i}^{(c)}$.

The ratios of single-to-coincidence electron and ion wave-packet widths, $\delta r_e^{(s)}/\delta r_e^{(c)}$ and $\delta r_i^{(s)}/\delta r_i^{(c)}$, can be considered as a measure of entanglement, as remarked at the beginning of this section. These ratios can be referred to as the electron and ion entanglement parameters in the form

$$R_e \equiv \frac{\delta r_e^{(s)}}{\delta r_e^{(c)}} \quad \text{and} \quad R_i \equiv \frac{\delta r_i^{(s)}}{\delta r_i^{(c)}}. \tag{36}$$

Entanglement is large if $R_e \gg 1$ and/or $R_i \gg 1$. If $R_e \approx 1$ and $R_i \approx 1$, there is little or no entanglement at all.

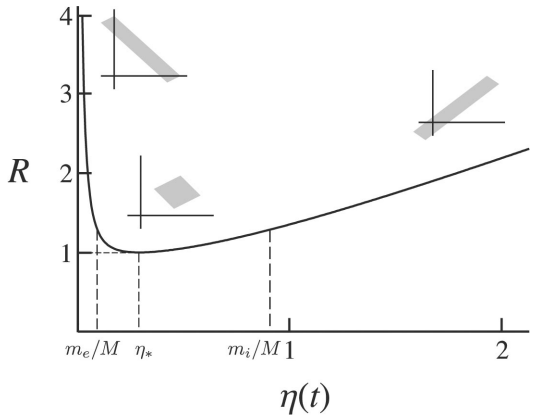

FIG. 4. Plot of the entanglement parameter R as a function of $\eta(t)$ with $m_e/m_i=0.1$; η_* is the stability point (42) at which $\eta(t) \equiv \text{const} = \sqrt{\mu/M}$. The insets give the corresponding plots of the one-dimensional analog $|\Psi(x_e,x_i,t)|^2$ from Fig. 2. The axes of the three insets have been rescaled so as to show the details more clearly. The regions where the entanglement parameter is large are clearly seen to correspond to a large aspect ratio of the shaded areas.

By using Eqs. (32)–(35), we can find a useful form for the ratios, when $R_e \approx R_i$, which we will denote simply R and refer to as the entanglement parameter:

$$R \equiv \sqrt{\eta + \frac{1}{\eta}\left(\frac{m_i}{M}\right)^2}\sqrt{\eta + \frac{1}{\eta}\left(\frac{m_e}{M}\right)^2}, \tag{37}$$

which is plotted in Fig. 4. Compared to the Schmidt correlation coefficient K the parameter R describes more detailed time-evolving features of entangled quantum states. In particular, in the coordinate picture that we use here, changes in the parameter R occur because of spreading of electron and ion wave packets after ionization. The relation (37) is actually valid only when $\eta \gg 1$ or $\eta \ll m_e/m_i$, and these are the regions where R is a good model for R_e and R_i, and $R \gg 1$. Even though R_e and R_i may not be exactly the same in the zone $m_e/M < \eta < 1$, they both have values around unity, $R_e \sim R_i \sim 1$. This is a very specific region, in which the electron-ion state is entangled in accordance with the general expression for the total wave function (4), but entanglement does not manifest itself in terms of R, i.e., in terms of the coincidence vs single-particle measurements.

The asymptotic behaviors of R in three different regions of $\eta(t)$ are particularly noteworthy:

$$\text{Region 1, } \eta \ll \frac{m_e}{M} \ll \frac{m_i}{M}\text{: } R \sim \frac{m_e m_i}{M^2}\frac{\Delta r_{\text{rel}}(t)}{\Delta r_{\text{c.m.}}(t)} \sim \left(\frac{\mu}{M}\right)\frac{1}{\eta(t)}; \tag{38}$$

$$\text{Region 2, } \frac{m_e}{M} \ll \eta \ll \frac{m_i}{M}\text{: } R \sim 1; \tag{39}$$

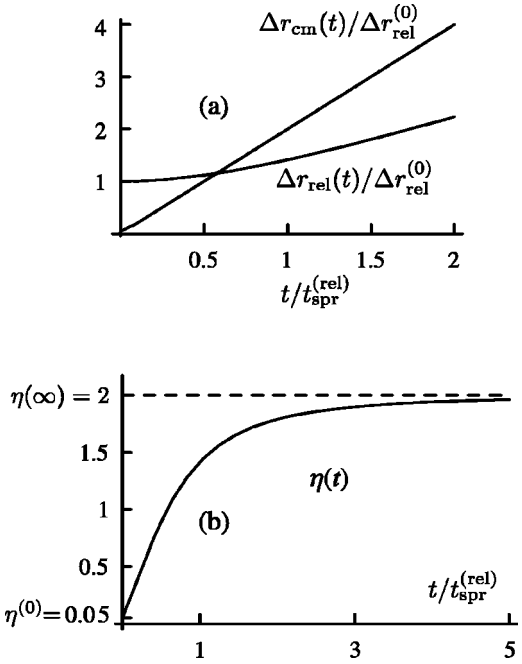

FIG. 5. (a) shows the time-dependent widths of the center-of-mass and relative-motion wave packets, in units of $\Delta r_{\text{rel}}^{(0)}$, and (b) shows the control parameter $\eta(t)$. We have taken $\eta_0=0.05$ and $m_e/M=0.1$.

$$\text{Region 3, } \frac{m_e}{M} \ll \frac{m_i}{M} \ll \eta\text{: } R \sim \eta(t). \tag{40}$$

Note that the minimal value of the entanglement parameter (36) is equal to 1, $R_{\min}=1$, and it is achieved at $\eta(t) = \sqrt{\mu/M}$.

V. TIME EVOLUTION OF PACKET WIDTHS AND ENTANGLEMENT PARAMETER

In Figs. 3 and 4 both the electron and ion wave-packet widths and the entanglement parameters are shown, for fixed t, in their dependence on the control parameter defined earlier:

$$\eta(t) = \frac{\Delta r_{\text{c.m.}}(t)}{\Delta r_{\text{rel}}(t)}. \tag{41}$$

However, we can use the same pictures to show the evolution of the widths $\Delta r_e(t)$ and $\Delta r_i(t)$ and the entanglement parameter defined in Eq. (37). To do this, we have to learn how $\eta(t)$ changes with time.

The two typical cases of significantly different behavior are illustrated in Figs. 5 and 6. Parts (a) and (b) of these figures show the time dependence of the widths $\Delta r_{\text{c.m.}}(t)$ and $\Delta r_{\text{rel}}(t)$ themselves and of their ratio, which equals $\eta(t)$. A key feature of $\eta(t)$ is its strong dependence on the initial sizes of the center-of-mass and relative-motion wave packets, $\Delta r_{\text{c.m.}}^{(0)}$ and $\Delta r_{\text{rel}}^{(0)}$, or in other words, on the initial value of the control parameter $\eta(0) \equiv \eta_0$. Depending on its initial

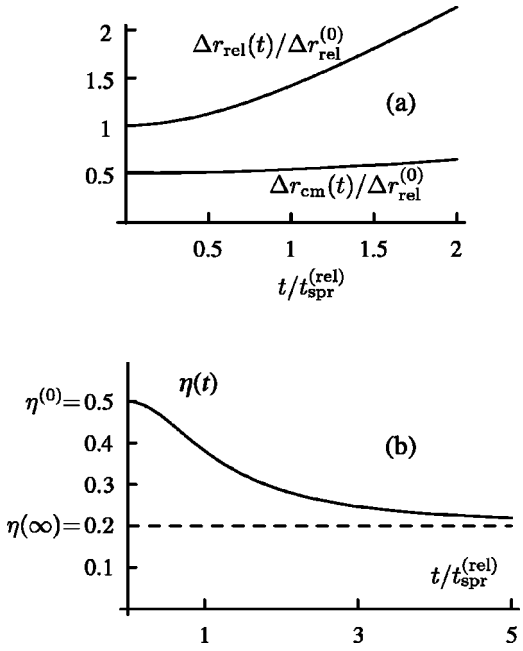

FIG. 6. The same as in Fig. 5 but with $\eta_0=0.5$.

value, η is either rising as shown in Fig. 5(a) or falling as in Fig. 6(b). The border between these two regimes is given by $\eta_0=\eta_*$, where

$$\eta_* \equiv \sqrt{\frac{\mu}{M}}. \tag{42}$$

If $\eta_0=\eta_*$, the center-of-mass wave packet spreads faster and eventually becomes wider than the relative-motion wave packet, although initially $\Delta r_{\rm c.m.}^{(0)} \ll \Delta r_{\rm rel}^{(0)}$. In this case the control parameter $\eta(t)$ is a monotonically growing function of t, as in Fig. 5(b). On the contrary, if $\eta_0>\eta_*$, the center-of-mass wave packet spreads more slowly than the relative-motion wave packet. Although initially the center-of-mass packet can be either narrower or wider than the relative-motion packet, at very large t the relative-motion packet becomes wider than the center-of mass packet. This gives rise to a falling function $\eta(t)$ shown in Fig. 6(b). In both cases ($\eta_0<\eta_*$ and $\eta_0>\eta_*$) the ranges of variation of the parameter $\eta(t)$ are finite. At very long times $\eta(t)$ has the asymptotic value

$$\eta \to \eta_\infty \equiv \frac{\mu}{M}\frac{1}{\eta_0}, \tag{43}$$

which follows directly from the definition of η (41) and Eqs. (9) and (25) for the widths $\Delta r_{\rm c.m.}(t)$ and $\Delta r_{\rm rel}(t)$. In the case $\eta_0=\eta_*$ the parameter $\eta(t)$ does not depend on time at all: $\eta(t)=\text{const}(=\eta_*=\eta_0=\eta_\infty)$.

By finding the evolution regimes for the control parameter $\eta(t)$, we can also draw definite and interesting conclusions on the evolution of the entanglement parameter R defined in Eq. (37). Directly from Eq. (37) one can easily see that for an arbitrary value of η the entanglement parameter obeys the relation

$$R\left(\frac{1}{\eta}\frac{\mu}{M}\right) \equiv R(\eta). \tag{44}$$

The initial and final values of η are connected with each other by exactly the same substitution as used in Eq. (44), and we see that the initial and final values of the entanglement parameter must be equal:

$$R_0 \equiv R_\infty = R(t\to\infty). \tag{45}$$

This equality is valid identically for all values of η_0. If η_0 is located in one of the high-entanglement regions of Fig. 4, $\eta_0 \ll \mu/M$ as in Eq. (38), or $\eta_0 \gg 1$ as in Eq. (40), the final value of η is in the opposite of these two high-entanglement regions, $\eta_\infty \gg 1$ or $\eta_\infty \ll \mu/M$.

Thus we see that $R(t)$ starts from a large value R_0, falls to $R\sim 1$, and then grows again to the same value from which it started. Physically such an evolution means that initially one of the wave packets $\Psi_{\rm rel}$ or $\Psi_{\rm c.m.}$ is much wider than the other one, and for this reason the entanglement-induced narrowing of the packets measured in the coincidence scheme is large. Then, as the narrower wave packet spreads faster, they will become approximately of the same width, and R decreases. Finally, when the initially narrower but faster-spreading wave packet outstrips the initially wider but slower-spreading one, the relation between their widths reverses, and this returns us to the initial case of a large entanglement-induced narrowing of the packets measured in coincidence.

The difference between the cases $\eta_0 \ll \mu/M$ and $\eta_0 \gg 1$ concerns only the direction of evolution, respectively, to the right or to the left on the η axis in Fig. 4. If the initial value of the parameter η is located in the small-entanglement region defined in Eq. (40), where $\mu/M<\eta<1$, all the conclusions about the direction of evolution and about the relation between the initial and final values of R remain valid. However, in this case R remains at the order of 1 at all times t. If $\eta_0=\eta_*$, we find simply the constant value $R(t)\equiv 1$.

VI. EXPERIMENTAL CONSIDERATIONS

The discussion as given so far does not treat some elements that will come into play in experimental tests. In order to bring them into focus briefly, we show in Fig. 7 what can be called experimentally realistic zones. We have plotted the region where the relative probability distribution is nonzero. It has a three-dimensional aspect that we do not need to show because it is axially symmetric about the polarization axis of the ionizing light beam, taken as the vertical axis here. It is not spherically symmetric because of the dipole character of photoionization contained in the factor $\vec{d}_{E_*0}\cdot\vec{\mathcal{E}}_0$ in Eq. (20). The crescent-shaped shaded areas indicate the regions where the relative-motion wave function $|\Psi_{\rm rel}(\vec{r}_e)|^2$ is relatively large.

Taking the time evolution of the relative wave function to be strictly limited by the step function $\theta(vt-r_{\rm rel})$, as in Eq. (20), we will here consider the ion position to define the origin of polar coordinates ($r_i\equiv 0$), in which case a circle of radius $r_e=vt$ limits the range of the electron coordinate at

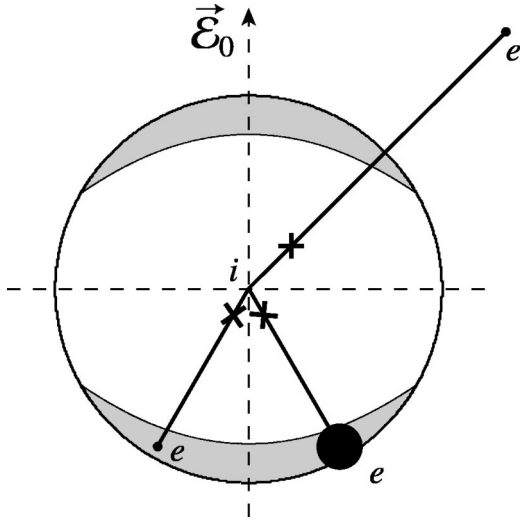

FIG. 7. Sketch showing relative influences of $|\Psi_{\rm rel}|^2$ and $|\Psi_{\rm c.m.}|^2$ on experimental measurements of localization. The ion is taken as the origin of coordinates, and Eq. (20) shows that a circle of radius $r_e = vt$ limits the range of the electron coordinate. The crescent-shaped shaded areas are the regions where the wave function $|\Psi_{\rm rel}|^2$ is relatively large (one-third of the maximum or more) at a given time t, and the sizes of the black spots indicate the widths of $|\Psi_{\rm c.m.}|^2$ for three different electron positions where experiments might be done. In each case a cross marks the corresponding center of mass. The black spots can take different sizes relative to the size of the shaded area depending on the value of the control parameter $\eta(t)$, as defined in Eq. (41). A large value of the entanglement parameter R is obtained for $\vec{r}_e$ located where there is a well-localized $|\Psi_{\rm c.m.}|^2$ (i.e., a small black spot) combined with a large value of $|\Psi_{\rm rel}|^2$. In the case when the black spot is located far outside the shaded area there is no overlap between $|\Psi_{\rm rel}|^2$ and $|\Psi_{\rm c.m.}|^2$ and the total wave function vanishes.

time t. The relative coordinate probability distribution $|\Psi_{\rm rel}(\vec{r}_e)|^2$ is of course not uniform inside this circle, so we have drawn the boundary on which $|\Psi_{\rm rel}|^2$ equals $\frac{1}{3}$ of its maximum value, shown as the two sectors with crescent shape. However, the probable position of the electron is also influenced by the c.m. wave function $|\Psi_{\rm c.m.}|^2$. In the figure the sizes of the black-spot regions show the ranges of electron positions given by $|\Psi_{\rm c.m.}(\vec{r}_e)|^2$ for different positions of the center of mass, which are indicated by crosses.

The figure has many variations, and the sizes of the crescent and Δr_e zones change in time, as our formulas indicate. The overall shapes will remain the same, and a generic high-entanglement experiment will be one that ensures overlap between a small black-spot region and a high-probability portion of one of the crescent regions (near the circle boundary). Higher count rates with reduced values of the entanglement parameter R will be associated with increased size of the black-spot region.

VII. PHOTODISSOCIATION

It is easy to see that very similar results will arise in a treatment of photodissociation of molecules. Here we remark briefly on some of the differences. Let us assume that we consider a diatomic molecule undergoing dissociation. There will be a relevant dissociation rate γ_D, which can be substituted for the γ_I governing ionization, and just as for the atom there will be an initial localization of the molecular center of mass. Then the main differences from the ionization example arise because the mass ratio of the fragments is much closer to 1. Compared to the case of photoionization, where $m_e \ll m_i$, the masses M_1 and M_2 of the photodissociation fragments obey $M_1 \sim M_2$.

Given this, the relative-motion velocity after dissociation $v \sim \sqrt{\omega/\mu}$ is significantly smaller than in the case of ionization, $v_{\rm mol} \sim \sqrt{\omega/M}$. The main difference between photoionization and photodissociation results concerns the region $\mu/M < \eta(t) < 1$ of intermediate values of $\Delta r_{\rm c.m.}(t)$ in Fig. 4 where $R \sim 1$. For $M_1 = M_2 = \frac{1}{2}M$ this region degenerates into a single point $\eta(t) = \frac{1}{2} = \eta_*$ [Eq. (42)]. The entanglement parameter R is large at both $\eta(t) < \eta_*$ and $\eta(t) > \eta_*$. To show more clearly the difference between photoionization and photodissociation, we plot in the right picture of Fig. 8 both molecular and atomic entanglement parameters in their dependence on $\ln(\eta)$, with the electron to ion mass ratio taking a realistic value $m_e/m_i \sim 10^{-4}$. This picture shows that if in the case of photoionization there is a rather large region of intermediate values of η where the entanglement parameter is not large, $R \approx 1$, in the case of photodissociation of a molecule the entanglement parameter is large practically at any η except the one point $\eta = \eta_*$.

In its dependence on time t the control parameter $\eta(t)$ changes in a way similar to that described above for photoionization: $\eta(t)$ grows if initially it is small ($\eta_0 < \eta_*$) and falls if large ($\eta_0 > \eta_*$). The final value of the control parameter η_∞ is related to η_0 by Eq. (43), which takes the form $\eta_\infty = 1/(4\eta_0)$. As shown previously, the initial and final values of the time-dependent parameter $R(t)$ are equal to each other, $R_0 = R_\infty$. At $\eta_0 = \eta_*$ both the control parameter $\eta(t)$ and the parameter $R(t)$ are constant with time t: $\eta(t) \equiv \eta_0$ and

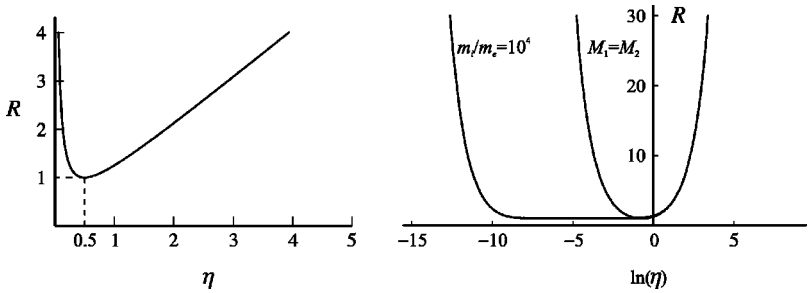

FIG. 8. Entanglement parameter R for two dissociating molecular fragments with $M_1 = M_2$ (left) and the same dissociation curve plotted vs $\ln(\eta)$ on the right, where the corresponding photoionization curve is included for comparison, with its very different mass ratio $m_i = 10^4 m_e$.

$R(t) \equiv 1$. This is the only case when there is no evolution of the entanglement parameter. In all other cases ($\eta_0 \neq \eta_*$) the entanglement parameter is large initially, drops to the value $R=1$ at such t that gives $\eta(t)=\eta_*$, and then grows until it reaches its initial value R_0.

VIII. CONCLUSION

We have evaluated the space-time behavior of the joint quantum state of an ion and electron following photoionization. Neglect of the incident photon momentum and of the final-state Coulomb interaction means that the evolution of the state, and thus of the entanglement between the two particles, is constrained only by free-particle two-body momentum and energy conservation. This evolution provides a calculable illustration of the situation involving massive particles sketched in the famous paper of Einstein, Podolsky, and Rosen [3]. We have obtained expressions for the entanglement-induced wave-packet narrowing that occurs, and have indicated how entanglement can be identified experimentally and quantitatively. To do this we introduced the entanglement parameter R, the ratio between the entanglement-free wave-packet width and the coincidence wave-packet width. This is effectively the degree of entanglement when entanglement is large, a relation to be examined further in a separate investigation [16]. We gave expressions for R in terms of ionization rate and packet-spreading velocity, which are of course themselves determined by underlying parameters such as atomic bound-free dipole moments, relative electron and ion masses, ionizing field strength, etc. It was shown that R depends in a simple way on the basic control parameter $\eta = \Delta r_{\mathrm{c.m.}}(t)/\Delta r_{\mathrm{rel}}(t)$, and can be much larger than unity in two limits, when $\eta \gg 1$ and also $\eta \ll 1$. The same formalism can be applied equally well to photodissociation of a diatomic molecule. For realistic physical values of the relevant parameters, in a typical example of atomic photoionization, R is not very large because of the extreme discrepancy between m_i and m_e, but for photodissociation of a diatomic molecule, where the fragment masses can be approximately equal, R can be substantially increased.

ACKNOWLEDGMENTS

We are pleased to acknowledge helpful conversations and correspondence with E.A. Shapiro and K. Wodkiewicz. The research reported here has been supported under the DoD Multidisciplinary University Research Initiative (MURI) program administered by the Army Research Office under Grant No. DAAD19-99-1-0215, NSF Grant No. PHY-0072359, Hong Kong Research Grants Council (Grant No. CUHK4016/03P), and the RFBR Grant No. 02-02-16400.

[1] K. Gottfried, *Quantum Mechanics* (Benjamin, New York, 1966), pp. 463–474.
[2] M. V. Fedorov, *Atomic and Free Electrons in a Strong Light Field* (World Scientific, Singapore, 1997).
[3] A. Einstein, B. Podolsky, and N. Rosen, Phys. Rev. **47**, 777 (1935).
[4] M. A. Nielsen and I. L. Chuang, *Quantum Computation and Quantum Information* (Cambridge University Press, Cambridge, England, 2000).
[5] A. Ekert and P. L. Knight, Am. J. Phys. **63**, 415 (1995).
[6] The Schmidt theorem is equivalent to the singular value decomposition in matrix theory. Mathematical details can be found, for example, in A. Peres, *Quantum Theory: Concepts and Methods* (Kluwer Academic Publishers, Dordrecht, 1995).
[7] J. H. Eberly, K. W. Chan, and C. K. Law, Proc. R. Soc. London, Ser. A **361**, 1519 (2003).
[8] K. W. Chan, C. K. Law, and J. H. Eberly, Phys. Rev. Lett. **88**, 100402 (2002); Phys. Rev. A **68**, 022110 (2003).
[9] K. W. Chan, C. K. Law, M. V. Fedorov, and J. H. Eberly, J. Mod. Phys. (to be published).
[10] H. Huang and J. H. Eberly, J. Mod. Opt. **40**, 915 (1993); C. K. Law, I. A. Walmsley, and J. H. Eberly, Phys. Rev. Lett. **84**, 5304 (2000).
[11] C. K. Law and J. H. Eberly, e-print quant-ph/0312088; Phys. Rev. Lett. (to be published).
[12] M. D. Reid and P. D. Drummond, Phys. Rev. Lett. **60**, 2731 (1988); M. D. Reid, Phys. Rev. A **40**, 913 (1989).
[13] T. Opatrny and G. Kurizki, Phys. Rev. Lett. **86**, 3180 (2001).
[14] L. D. Landau and E. M. Lifshitz, *Quantum Mechanics* (Pergamon Press, Oxford, 1977).
[15] A. V. Rau, J. A. Dunningham, and K. Burnett, Science **301**, 1081 (2003).
[16] Rules for breakup processes, explicitly joining localization measurements to a Schmidt analysis, will be treated elsewhere.